UNIVERSITY OF CALIFORNIA, IRVINE

Characterization and Analysis of Conductance: From Polymers to Single Electrons

THESIS

submitted in partial satisfaction of the requirements for the degree of

MASTER OF SCIENCE

in Chemistry and Material Physics (ChaMP)

by

Nicholas Tallarida

Thesis Committee:

Professor V.A. Apkarian, Chair

Professor Nien-Hui Ge

Associate Professor Eric Potma

2016

Contents

List of Figures

List of Tables

Acknowledgments

I would like to express my deepest appreciation to my advisor, Professor Ara Apkarian, who has provided me with the opportunity, guidance, and support to develop as a scientist. I would like to thank my committee members, Professor Nien-Hue Ge and Professor Eric Potma for their advice and support throughout my graduate career. Furthermore, I'd like to thank Dr. Joonhee Lee for his tireless support, unparalleled patience, and invaluable expertise, without whom this research would not have been possible. Lastly, I'd like to thank the rest of the Apkarian Lab, especially Laura Ríos, for being helpful and understanding.

I also thank ACS Publications for permission to include parts of chapter 2 and 3 of my dissertation, which was originally published in the Journal of Physical Chemistry C and ACS Nano.

Financial support was provided by the Center for Chemistry at the Space-Time Limit funded through NSF (CHE-0802913).

Abstract of the Thesis

Characterization and Analysis of Conductance: From Polymers to Single Electrons

By Nicholas Tallarida

Master of Science in Chemistry and Material Physics

University of California, Irvine, 2016

Professor V.A. Apkarian, Chair

Experimental studies on the conductive properties of molecular systems led to the discovery and characterization of two essential elements of molecular electronics: a molecular wire and a single electron switch. The synthesis and cyclic current versus voltage (I/V) measurements of intrinsically conductive linear chain [-Ag-S-BP-S-]$_n$ polymers determined their relatively large conductivity and suggested that mobile Ag adatoms on the roughened Ag surface catalyzed the polymerization. On the other hand, the single electron switch was determined to be controlled by the spin-vibronic density of an odd electron on a single molecule. Analysis of the two-level telegraphic conductance switching produced effective wiring diagrams to control the switch's frequency, amplitude, polarity, and duty-cycle. Furthermore, it gave insight into the molecule's governing vibronic Hamiltonian.

Introduction

Due to the large variety of potential technological applications for conductive polymers, optimizing their useful properties, such as conductivity, robustness, and processibility, is of great interest to researchers.[1] Trans-polyacetylene is a well-known and studied organic polymer, with an intrinsic conductivity of only 10^{-2}-10^{-3} S m^{-1}. However, through various oxidative or reductive doping methods, it's conductivity can be improved by up to seven orders of magnitude.[2] Carbon nanotubes and graphitic sheets potentially provide a means to shrink the scale of electronic components but have so far been limited by their processibility.[3,4] The need for novel bottom-up designs of molecular circuitry, however, makes the self-assembly nature of polymers desirable.[5] Moreover, recent advancements made in the production of metallo-organic polymers has demonstrated the method's ability to produce conductivities as high as 10^4 S m^{-1}.[6] The processibility of molecular wires and sheets provide a potential pathway towards the miniaturization of electronics. In this regard, a new surface-assembled intrinsically conductive organo-silver linear chain polymer, which we discovered, holds great promise given a more complete understanding of its growth and conductive properties.

However, to realize the spatial limit of electronics, electronic circuit elements also need to be shrunk. The idea that single molecules can act as functional circuit elements[7] spurred research into a variety of molecular components including single molecule transistors[8], rectifiers[9], and switches[10–12]. The ability to control the conductance at the atomic scale is highly desirable. Schirm *et al.* demonstrated a reliable and robust two-terminal atomic conductivity switch. The observed hysteretic behavior provides the ability to use the system

as a single-atom memory element.[13] Kumagai *et al.* explored the intramolecular hydrogen transfer in a porphycene molecule, observing that this tautomerization is strongly dependent on the molecule's local environment.[14] The ultimate limit in miniaturization of electronics can be regarded as that of a single functional electron, as opposed to a molecule. Moreover, to maximize utility of nanoscopic devices by very-large-scale integration, it is important to minimize the generation of heat due to various dissipation channels that may be associated with the operation of the circuit element.[15] The conductivity switch, which we demonstrate using an unpaired radical electron on a single Zn-etioporphyrin molecule, meets these requirements. It relies on the spin-flip of one electron in one molecule, with energy spacing between spin-vibronic states of 1 meV.

Investigations on the single electron switch, requiring the capability to measure submolecular electron dynamics with millisecond time resolution, demonstrate the power of scanning tunneling microscopy (STM) for single molecule studies. Despite having the necessary spatial resolution, the ms time resolution of STM, and other electron probe microscopies, is not high enough to capture the ultrafast nuclear and electron dynamics within a single molecule. Alternatively, the advent of femtosecond lasers[16] has enabled the study of ultrafast molecular dynamics albeit without the same degree of spatial resolution.[17,18] Successfully coupling these techniques would allow for the study of atomic and electronic motions on their relevant time and space scales. An ultrafast laser-coupled STM offers one promising method for exploring this regime.[19,20]

Obtaining single-molecule sensitivity with optical approaches is challenging, requiring significant enhancement of the local electric field felt by the molecule.[21] Plasmonically active nanostructures, like metallic nanoparticles or tips, provide an efficient way of creating locally enhanced optical fields, or hot spots, boosting the sensitivity of optical spectroscopies toward the single molecule limit.[22] Surface-enhanced Raman spectroscopy (SERS) and tip-enhanced Raman spectroscopy (TERS) are two techniques that make full use of enhanced local field produced by metallic nanostructures. By illuminating the tip-sample juction of

a STM, TERS can provide chemical information to compliment the STM's spatial resolution[22]. The high optical field enhancements produced at the apex of the STM tips enables optical spectroscopy below the diffraction limit.

Successes with this approach have mainly been limited to relatively large but bright dye molecules like R6G[23] and BCB[24] through electronically resonant Raman, with the highest spatial resolutions ranging from 3 to 15 nm[25]. A notable exception is the sub-nanometer spectroscopic resolution achieved by Zhang *et al.* on a single porphyrin molecule.[25] Such high spatial resolution is attributed to spectrally matching the resonance of the nanocavity plasmon to the molecule's vibronic transitions. Additionally, Lee *et al.* demonstrate sub-nanometer spectral resolution on a single molecule by measuring the emitted electroluminescence (EL) signal. Utilizing the phase information contained within the EL spectrum's Fano line profiles, it is possible to extract femtosecond time information.[26] The progresses made toward achieving single molecule spectroscopic resolution and the improvements in experimental apparatus and plasmonic tip production are discussed below.

Chapter 1

Conductive Self-Assembling Polymer

Conductive polymers have proven themselves to be extremely useful for a variety scientific and technological applications and has become the target of research endeavors[1]. One of the fundamental pushes in this field is to combine the processibility common to the more well-studied organic intrinsically-conductive polymers like that of trans-polyacetylene[2] with the potential electrical properties of structures like carbon nanotubes or graphitic sheets.[3,4] In an effort to produce and study self-assembled monolayers of biphenyl-4,4'-dithiol (BPDT) on a roughened silver substrate for the use in unrelated investigation of nano-scale chemistry, a metallo-organic polymer with an intrinsic conductivity of 2 to 3 orders of magnitude larger than some of the best organic polymers was produced.

On the roughened silver surface, BPDT surprisingly forms large ($> 1\ \mu$m) surface-assembled polymers (SAPs) as opposed to the well characterized self-assembled monolayers that it forms on flat silver and gold surfaces.[27] The SAPs synthesis procedure was originally based on the typical SAM synthesis[27] and was subsequently refined by a former lab member, Stephen Sasaki. With the help of various lab members, SAPs were prepared and characterized[28]. The substrates, Ag tips, were prepared by electrochemical etching. A 500 μm diameter silver wire was cut into 15 mm lengths. Roughly 3 mm of the wire was submerged into a 1:1:1 H_2O_2:CH_4OH:NH_4OH (30%, 100%, 30%) bath along with a PtIr cathode. A 15 V potential

electrochemically etches the silver wire into a tip with a 1-50 μm radius of curvature. The tip was rinsed with ethanol and dipped into concentrated hydrofluoric acid to remove any surface oxides and/or residues.

To prepare the SAP, a freshly prepared tip was first sonicated in fresh ethanol twice for 15 mins each. Meanwhile, a saturated solution of BPDT in ethanol was prepared and sonicated for 30 mins. The cleaned tip was immersed in the BPDT solution for 24-168 hrs. After this growth period, the tip was removed from the solution and once again sonicated in fresh ethanol twice for 15 mins each.

As shown in Figure 1.1, freshly polymerized Ag tips were readily imaged using scanning electron microscopy (SEM). The ease with which the SAPs were imaged with electron beams indicate their conductivity. Energy-dispersive X-ray spectroscopy (EDS) was used to determine the atomic composition of the polymer chains, determining a 2:1 S:Ag ratio, suggesting that the polymer sheets and chains were composed mainly of S-Ag-S covalent linkages, consistent with linear polymeric chains of [-Ag-S-BP-S-]$_n$. Furthermore, it was determined that the samples do not measurably oxidize, even after spending weeks in ambient conditions.

Further experiments were conducted in an attempt to correlated the surface morphology of the etched silver tips with the habit of the polymer growth. Tips were produced with varying degrees of surface roughness through electrochemical etching, giving morphologies ranging from flat to cubic crystalline. Upon growing SAPs on these tips, no correlation between the resulting habits and the orginal surface morphologies could be made. Nevertheless, DFT analyses done by R.Q. Wu and Y.N. Zhang demonstrated the importance of silver adatoms in the construction of linear chains of [-Ag-S-BP-S-]$_n$. These results suggest that Ag adatoms, which are mobile on the surface at room temperatures, instigate the growth of linear polymer chains. The size of the polymer sheets may be indicative of the Ag adatom concentrations on the surface. The high surface converges of the growths, however, likely prevent free BPDT from diffusing to the adatoms on the surface.

Ultimately, the conductivity of the metallo-organic polymer was confirmed using an am-

bient STM. A gold metal tip was used to record cyclic current-voltage (I/V) curves on a heavily polymerized etched silver wire. Topography scans verify that the surface was highly corrugated with 500 nm changes in the height over a small lateral displacement of 1 μm, supporting the formation of densely packed polymer. The cyclic I/V curves (Fig. 1.1) reveal a HOMO-LUMO gap of $\sim$1.8 V, independent of the tip location. The instrument saturates as the bias was ramped up around +1.3 V and remains as such until a nearly ohmic response was seen between $\pm$0.5 V. The hysteresis seen in these curves suggest that the junction was flipping between conductive and insulating states due to the formation and breaking of sulfur-gold bonds.[29] The effective resistance of the ohmic junction ranges from 7 to 22 MΩ. This range could result from the $\pm$100 nm vertical displacement of the tip when the feedback was momentarily activated between subsequent curves, giving an estimated conductivity of 1-10 S/m.

The high conductivity and ease at which this polymer assembles makes it a potential candidate for bottom-up molecular electronic circuitry.[5] It could potentially be used to bridge silver contacts on electronic boards by chemical etching of the silver contacts or by catalyzed-assembly due to point defects. At any rate, the conductive wires and sheets of this polymer stands as a potential alternative to nanotubes and graphitic sheets for a variety of applications.

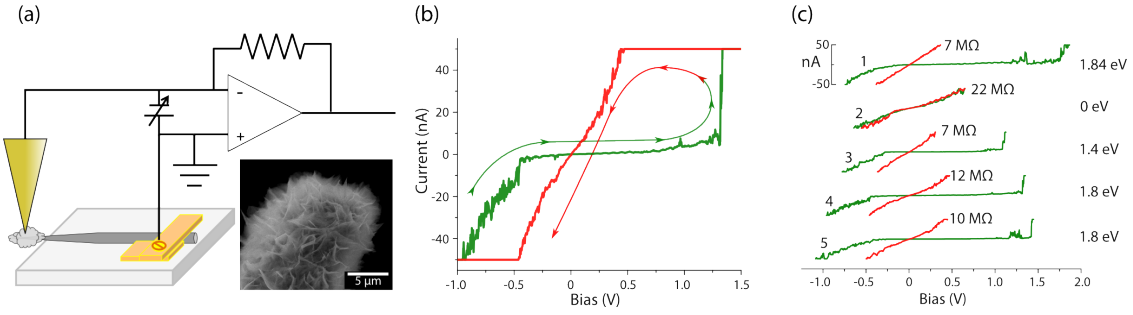

Figure 1.1: Conductivity of SAPs. (a) Schematic of the experimental setup for the conductivity measurement. (inset) SEM image shows typical SAP growth on the etched region of the wire. (b) Typical cyclic I/V curve showing the onset (red) of ohmic behavior. (c) Additional I/V curves with their effective resistances and HOMO-LUMO bandgap. Reprinted with permission from reference [28]. Copyright 2014, American Chemical Society.

Chapter 2

Single Electron Switch

While intrinsically-conductive polymers represent one route towards molecular electronics via the production of molecular wires and sheets, a molecular switch using the most basic elements of a single molecule would represent the ultimate limit in molecular electronics. Researchers have approached this limit through the demonstration of single-atom memory elements and switches using inter-molecular atomic rearrangements.[13,14] The switch described in the following sections relies not on the motion of atoms but on the properties of a single unpaired electron. Furthermore, by forgoing "large"-scale motions of atoms, heat generation, which is one of the major problems facing Moore's Law, is minimized.

2.1 Experiment and Discussion

A single Zn-etiopophyrin radical anion ($ZnEtio^-$) isolated in the double-barrier, cryogenic, ultra-high vacuum scanning tunneling microscope (UHV-STM) junction at 5 K and 2×10^{-11} torr, displays an interesting switching behavior[30]. To prepare the system, neutral ZnEtio is sublimed onto a thin aluminum oxide layer grown on an atomically flat NiAl(110) surface. The ZnEtio molecule is reduced to form $ZnEtio^-$ by injecting electrons at a junction basis > 0.7 V. Constant current topographic scan of the stable radical anion reveals the molecule's anisotropic clover-like appearance, composed of 4 distinct lobes (Fig. 2.1). As

the junction bias is ramped, along with previously understood electroluminescence[26], bistable conductance switching is observed. The onset of switching, 1.8 V, corresponds to the access of both the dianion state of the molecule, ZnEtio^{2-}, and the conduction band of the oxide.

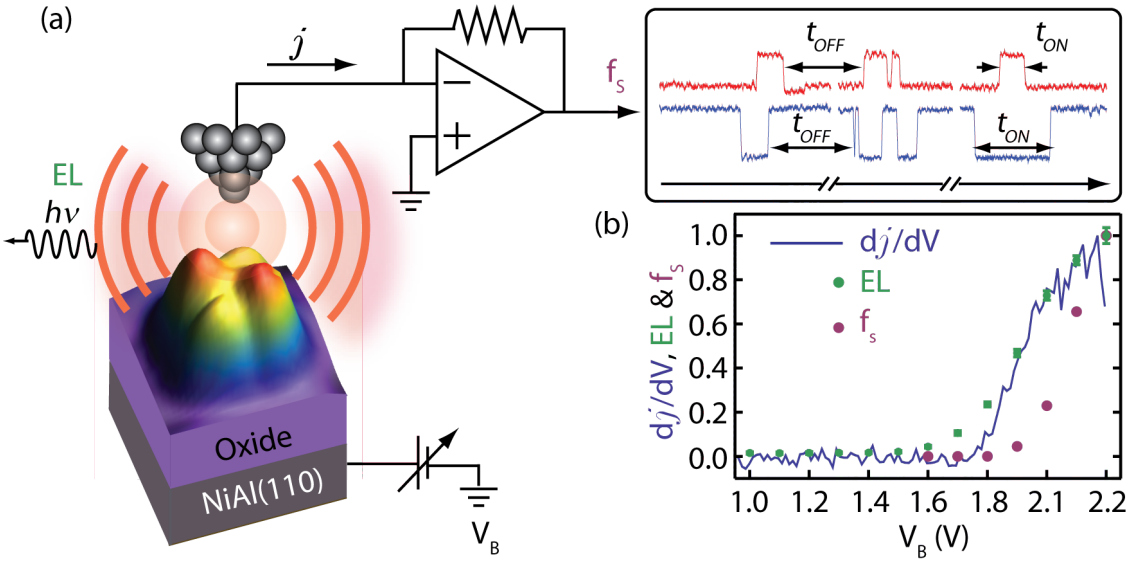

Figure 2.1: ZnEtio^{-} conductance switch. (a) Schematic of the setup with typical pre-resonant current-traces showing position dependent dichotomous positive (red) and negative (blue) switching. (b) The normalized dj/dV vs V_b curve, EL photon counts, and the switching rate (f_s) all follow the same resonant behavior associated with the onset of the dianion resonance at around 1.8 V. Reprinted with permission from reference [30], Copyright 2014 American Chemical Society.

Although this switching behavior was known within the lab prior to my involvement, additional measurements with a higher temporal resolution were needed. To characterize the kinetics of the switching behavior, current-time traces (with the feeback turned off at a sample bias (V_b) = 2.0 V) were recorded at 4 different tip placements, T_1-T_4, within the molecule (Fig. 2.2a). The current dependence of the process was analyzed by recording 60-second long traces with a 10 μs resolution at setpoint currents ranging from 15 to 70 pA. Additionally, a bias ramp, from 1.6 to 2.2 V, was done at a setpoint current of 20 pA to obtain the switching frequency, f_s, curve shown in Figure 2.2b. Since switching events at lower biases are longer and less frequent, 5-minute long traces with a 1-millisecond resolution were recorded at biases $<$ 1.9 V.

Figure 2.2 summarizes the data that characterizes the switching kinetics. The DC set-point is defined as the "off" $\equiv 0$ state and the transient state is defined as the "on" $\equiv 1$ state. The switching rates for any of the single position measurements is modeled by first order kinetics:

$$0 \rightarrow 1; \quad r_+ = j_0\sigma_{01} + k_{01} \tag{2.1a}$$

$$1 \rightarrow 0; \quad r_- = j_1\sigma_{10} + k_{10}, \tag{2.1b}$$

where $j_{0/1}$ is the current level (electrons s^{-1}) of the off/on state, σ_{nm} is the probability (transitions per electron) that a tunneling electron triggers the transition from state n to m, and k_{nm} is the spontaneous switching rate constant (s^{-1}) for transitions from state n to m. The amplitude of the switch is a function of tip placement,

$$\delta j(x, y) \equiv j_1(x, y) - j_0, \tag{2.2}$$

which is readily seen by polarity differences between the 4 tip placements. T_1 and T_3 have a positive amplitude while T_2 and T_4 have a negative amplitude. Whenever switching frequencies are within the gain-bandwidth of the current preamplifier (800 Hz at 10^{10} gain), the measured pulse height distrubution (Fig. 2.2c) is bimodal. However, if the on-time for the switch approaches the response time of the preamplifier, as it does at T_1 and T_3, corrections need to be made to obtain the true height and on-time of the switch. A piecewise deconvolution of the pulse shapes accounts for the response function of the amplifier, allowing the original signal to be extracted.

With these corrections, the dichotomy of all switching events is confirmed. Additionally, reducing the bias lowers the switching frequency and increases on-times, producing bimodal pulse height distributions (PHDs) for all tip placements.

Discriminator levels are used to create the residence time histograms (Fig. 2.2e,f), that

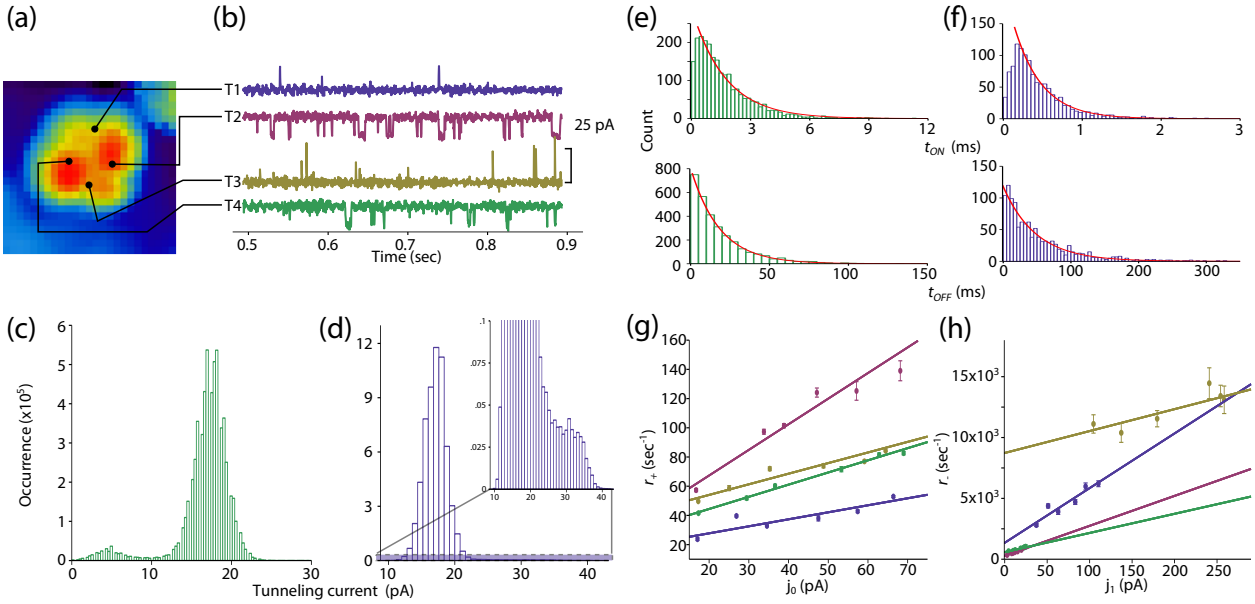

Figure 2.2: High-resolution switching analysis. Time traces recorded at $V_b = 2.0$ V and $j_0 = 20$ pA for 4 different tip placements (a) are vertically offset for clarity (b). (c) Pulse height distributions (PHD) at T4 is bimodal, indicating dichotomous negative switching. (d) PHD at T1 is broadly distributed due to the instruments response time. (e,f) Histograms for on/off-times have an exponential dependence, characteristic of a Markovian process. The peak seen at non-zero t_{ON} (f,top) is mostly due to under-counting short switches due to instrument limitations. (g,h) r_+ and r_- are linearly dependent on j_0 and j_1, respectively. Reprinted with permission from reference [30], Copyright 2014 American Chemical Society.

show an exponential probability density, $P_{0/1}$, characteristic of Markovian processes:[31]

$$P_{0/1} = \frac{1}{\tau_{0/1}} \exp(-t/\tau_{0/1}), \qquad r_{+/-} \equiv 1/\tau_{0/1} \tag{2.3}$$

As shown in Eq. 2.1 and Fig 2.2g,h, the rates obtained from fitting Eq. 2.3 to the resident time distributions are linearly dependent on the current, $j_{0/1}$, with intercepts and slopes giving k_{nm} and σ_{nm}, respectively. The extracted parameters are summarize in Table 2.1.

Even at 5 K, Table 2.1 shows a finite, position-independent probability for the molecule to spontaneously switch "on" in the projected limit of $j = 0$: $k_{01} \approx 30$ s^{-1}. In contrast, the spontaneous relaxation rate k_{10} is highly dependent on tip placement with rates that are 1 to 2 orders of magnitude larger than k_{01}. Since it is established that this is a two-level system, the observed variation amongst k_{10} is most likely due to perturbation by the tip. Higher

T	k_{01}, s^{-1}	$\sigma_{01}, (\times 10^{-6}/\mathrm{e}^{-})$	k_{10}, s^{-1}	$\sigma_{10}, (\times 10^{-6}/\mathrm{e}^{-})$
1	18.1±5	0.0769±0.02	1570±500	6.29±1
2	32.3±8	0.280±0.03	283±6	3.94±0.1
3	39.5±4	0.116±0.02	4380±3000	12.3±3
4	27.8±2	0.141±0.006	585±9	2.51±0.3

Table 2.1: Stimulated transmission probabilities (σ_{nm}) and spontaneous rate constants (k_{nm}) for the 4 tip positions. The uncertainties are the standard errors from the linear fits. Reprinted with permission from reference [30], Copyright 2014 American Chemical Society.

currents equate to smaller tip-molecule distances, leading to perturbation effects. If such effects could be eliminated, a single excited state lifetime, $1/k_{10}$, would be expected across all tip positions. Through detailed balance, the energy difference between the two levels is extracted,

$$\Delta E = k_B T \ln(k_{10}/k_{01}). \tag{2.4}$$

At negative switching locations, T_2 and T_4, $\Delta E = 0.94$ and 1.3 meV, respectively, while at positive switching locations, T_1 and T_3, $\Delta E = 1.9$ and 2.0 meV, respectively. Tip perturbation at positive switching positions are on the same order of magnitude as the energy level difference itself, ~ 1 meV. This small energy level difference, and the corresponding change in the topography, is observable with the STM and signifies a topography determined by vibronic density[32].

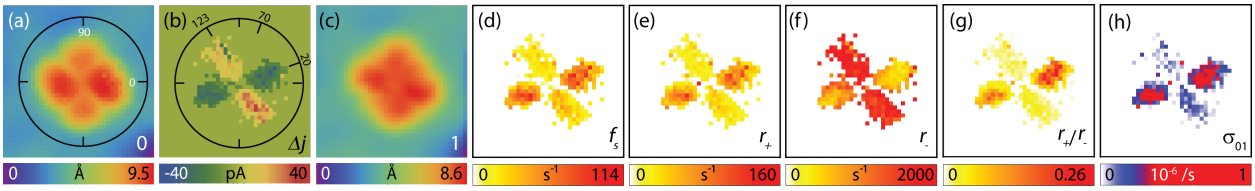

Figure 2.3: (a) Constant current topography of state 0. (b) Switch amplitude amp. (c) Extracted constant current topography of state 1. (d-h) Derived functional image maps of the frequency, "on"-rate, "off"-rate, duty cycle, and transition probability, respectively. Reprinted with permission from reference [30], Copyright 2014 American Chemical Society.

This same analyses were then carried out on each pixel of a 38x38 grid to determine the

full spatial dependence of the switch, producing functional images (Fig. 2.3). Each pixel is the result of a 2-second trace with 500 μm resolution. As implied by T_1-T_4, the amplitude map has zones of positive and negative conductance switching (Fig. 2.3b). Interestingly, the polarity changes from positive to nuetral to negative as the polar angle is changed from 123° to 70° to 20°, respectively, acting as three-throw bipolar rotary switch.

Understanding that the amplitude of each switch corresponds to the change in the topography between the two states, the δj map and the state 0 image (Fig. 2.3a) are used to calculate the transient state 1 constant current image (Fig. 2.3c). Since tunneling current is given as[33]

$$j = j_0 \exp(-2\kappa(z - z_0)), \tag{2.5}$$

the topography of the "on" state at the setpoint j_0, $Z_1(x,y)|_{j_0}$, is defined as

$$Z_1(x,y)|_{j_0} = Z_0(x,y)|_{j_0} - \frac{1}{2\kappa}\ln(\frac{j_0 + \delta(x,y)}{j_0}), \tag{2.6}$$

where j_0 is the current at the reference point z_0 and $\kappa = 1$ Å^{-1}. The resulting image, Figure 2.3c, shows that the vibronic density is rotated with respect to that of state 0, and is more evenly distributed across the four lobes. Thus, despite the fact that it takes our instrument ~2 minutes to record a topographic image (Fig 2.3a), the above transformation provides an estimated topography for a state with a ms lifetime.

Figures 2.3d-h show the functional images of the switching frequency, transition rates "on" and "off", duty cycle r_+/r_-, and probability σ_{01}. Coupled with the δj map, these functional images provide the required information to predict and control the polarity, frequency, amplitude, and duty cycle of this conductance switch. Furthermore, Fig 2.3a and 2.3c provide the spatial distribution of the vibronic densities of the initial and final states.

It is surprising that the excited state has such a long lifetime, $1/k_{10} \approx 1$ ms, despite being characterized by only a 1 meV energy difference. This suggests that the transition is

a forbidden process, specifically the spin-flip of the odd electron in the ZnEtio$^-$ radical. The spin-orbit coupling needed to break the spin degeneracy in ZnEtio$^-$ has been estimated to create a splitting of 0.1 meV,[34] an order of magnitude smaller than our observations. Vibronic distortions[35] and conical intersections, however, strengthen the coupling and increase the splitting, respectively, resulting in vibronic splittings of around 1 meV for aromatic molecules like benzene and butadiene[36], in line with the current observations.

2.2 Laplace Transform

The residence time, $t_{ON/OFF}$, is defined as the time spent in a particular state, on (1) or off (0), before switching away from it (Fig. 2.4). On up-switching lobes, t_{ON} is often on the order of our preamplifier rise-time, $\tau_{rise} = 450\ \mu s$, especially at resonant conditions. Here, τ_{rise} is the time it takes to rise from 10% to 90% of the input impulse signal. Since we assume that the switching behavior is impulsive, with instantaneous changes in conductivity (square pulse) relative to the response time of our electronics, the output signal is a convolution of our preamplifier's response function and this square pulse input.

Despite its complexities, the preamp can be viewed as a simple RC circuit. A RC circuit converts a square pulse input current, $I(t)$, into a time-dependent voltage signal, $V_0(t)$.

$$I(t) = \frac{v_0(t)}{R} + C\frac{d\,v_0(t)}{d\,t} = h[u(t-a) - u(t-b)] + m, \tag{2.7}$$

where h is the magnitude of the current step, m is the level of the "off" state, a and b are the start and stop times of the switch ($b > a$), $v_0(t)$ is the preamplifier's output voltage,

R is the circuit's resistance (gain), C is the circuit's capacitance, and

$$u(t-a) = \begin{cases} 1 & \text{if } t > a \\ 0 & \text{if } t < a \end{cases} \tag{2.8}$$

This linear differential equation can be solved using Laplace transforms.

$$\mathcal{L}\{v_0(t)\} = V_0(s) \tag{2.9}$$

$$\mathcal{L}\{1\} = \frac{1}{s} \tag{2.10}$$

$$\mathcal{L}\{\mathrm{e}^{at}\} = \frac{1}{s-a} \tag{2.11}$$

$$\mathcal{L}(f') = s\mathcal{L}(f) - f(0) \tag{2.12}$$

$$\mathcal{L}\{f(t-a)u(t-a)\} = \mathrm{e}^{-as}F(s) \tag{2.13}$$

$$\mathcal{L}^{-1}\{\frac{1}{s}F(s)\} = \int_0^t f(\tau)\,\mathrm{d}\tau \tag{2.14}$$

Take the Laplace transform of the middle and right hand side of Eq (2.7) using Eq (2.9-2.13).

$$\mathcal{L}\{\frac{v_0(t)}{R} + C\frac{d\,v_0(t)}{d\,t}\} = \mathcal{L}\{h[u(t-a) - u(t-b)] + m\} \tag{2.15}$$

$$\frac{1}{R}\mathcal{L}\{v_0(t)\} + C\,\mathcal{L}\{\frac{d\,v_0(t)}{d\,t}\} = h\big[\mathcal{L}\{u(t-a)\} - \mathcal{L}\{u(t-b)\}\big] + m\,\mathcal{L}\{1\} \tag{2.16}$$

$$\frac{V_0(s)}{R} + C\Big[sV_0(s) - v_0(0)\Big] = h\left[\frac{\mathrm{e}^{-as}}{s} - \frac{\mathrm{e}^{-bs}}{s}\right] + \frac{m}{s} \tag{2.17}$$

$$V_0(s)\left[\frac{1}{R} + C\,s\right] = h\left[\frac{\mathrm{e}^{-as}}{s} - \frac{\mathrm{e}^{-bs}}{s}\right] + \frac{m}{s} \tag{2.18}$$

Here, it is assumed that $v_0(0) = 0$. After solving for $V_0(s)$, use Eq (2.13) and (2.14) to

inverse Laplace Transform the equation back again.

$$V_0(s) = \left[\frac{1}{\frac{1}{RC}+s}\right]\frac{h}{C\,s}\left[\mathrm{e}^{-as} - \mathrm{e}^{-bs} + \frac{m}{h}\right] \tag{2.19}$$

Remembering

$$\mathcal{L}^{-1}\{\frac{1}{s}F(s)\} = \int_0^t f(\tau)\,\mathrm{d}\tau = \int_0^t \mathcal{L}^{-1}\{F(s)\}\,\mathrm{d}\tau\,, \tag{2.20}$$

$$\tag{2.21}$$

we can use it to show

$$\mathcal{L}^{-1}\{V_0(s)\} = \mathcal{L}^{-1}\{\frac{1}{s}\left[\frac{1}{\frac{1}{RC}+s}\right]\frac{h}{C}\left[\mathrm{e}^{-as} - \mathrm{e}^{-bs} + \frac{m}{h}\right]\} \tag{2.22}$$

$$v_0(t) = \int_0^t \mathcal{L}^{-1}\left\{\left[\frac{1}{\frac{1}{RC}+s}\right]\frac{h}{C}\left[\mathrm{e}^{-as} - \mathrm{e}^{-bs} + \frac{m}{h}\right]\right\}\mathrm{d}\tau \tag{2.23}$$

Eq (2.13) can be rewritten as

$$\mathcal{L}\{F(s)\}_{\tau-a}\,u(t-a) = \mathcal{L}^{-1}\{\mathrm{e}^{-as}F(s)\}, \text{ where} \tag{2.24}$$

$$F(s) = \frac{1}{\frac{1}{RC}+s} \tag{2.25}$$

The integrad in Eq (2.23) can then be simplified using Eq (2.11) and (2.24)

$$v_0(t) = u(t-a)\int_0^t \frac{h}{C}\mathrm{e}^{-\frac{\tau-a}{RC}}\mathrm{d}\tau - u(t-b)\int_0^t \frac{h}{C}\mathrm{e}^{-\frac{\tau-b}{RC}}\mathrm{d}\tau + \int_0^t \frac{h}{C}\frac{m}{h}\mathrm{e}^{-\frac{\tau}{RC}}\mathrm{d}\tau \tag{2.26}$$

$$v_0(t) = \int_a^t \frac{h}{C}\mathrm{e}^{-\frac{\tau-a}{RC}}\mathrm{d}\tau - \int_b^t \frac{h}{C}\mathrm{e}^{-\frac{\tau-b}{RC}}\mathrm{d}\tau + \int_0^t \frac{h}{C}\frac{m}{h}\mathrm{e}^{-\frac{\tau}{RC}}\mathrm{d}\tau \tag{2.27}$$

$$v_0(t) = \begin{cases} mR(1 - e^{-\frac{t}{RC}}) & \text{if } 0 < t < a \\ hR(-e^{-\frac{t-a}{RC}}) + mR(1 - e^{-\frac{t}{RC}}) & \text{if } a < t < b \\ hR(-e^{-\frac{t-a}{RC}} + e^{-\frac{t-b}{RC}}) + mR(1 - e^{-\frac{t}{RC}}) & \text{if } t > b \end{cases} \tag{2.28}$$

where RC, the time-constant of our preamplifier, is roughly $2.2/\tau_{rise} \approx 0.2ms$. Here, R represents the amplifier's gain ($10^{10}\, V/A$).

This equation can be rewritten to better conform with variables defined previously. Here, j_1 is the "on" level, j_0 is the "off" level or setpoint current, and τ is the preamplifier's time-constant.

$$v_0(t) = \begin{cases} j_0(1 - e^{-\frac{t}{\tau}}) & \text{if } 0 < t < a \\ (j_1 - j_0)(-e^{-\frac{t-a}{\tau}}) + j_0(1 - e^{-\frac{t}{\tau}}) & \text{if } a < t < b \\ (j_1 - j_0)(-e^{-\frac{t-a}{\tau}} + e^{-\frac{t-b}{\tau}}) + j_0(1 - e^{-\frac{t}{\tau}}) & \text{if } t > b \end{cases} \tag{2.29}$$

Figure 2.4 shows that as the length of the input step pulse approaches the time-constant of the preamplifier, the $v_0(t)$ fails to reach the true peak height. The preamplifier, not the system itself, is responsible for the ill-defined "on" state. By fitting individual peaks to equation 2.29, the true height of the step pulses can be extracted (Fig. 2.5).

The response of the preamplifier also affects the measured residence times. Typically, residence times are measured by calculating the time it took a step-function to pass above and then below a discriminator level. For a detector with an instantaneous response, this would be perfectly adequate. If, however, the detector as a finite response time, errors begin to develop. If the response time approaches the residence time, errors can approach and

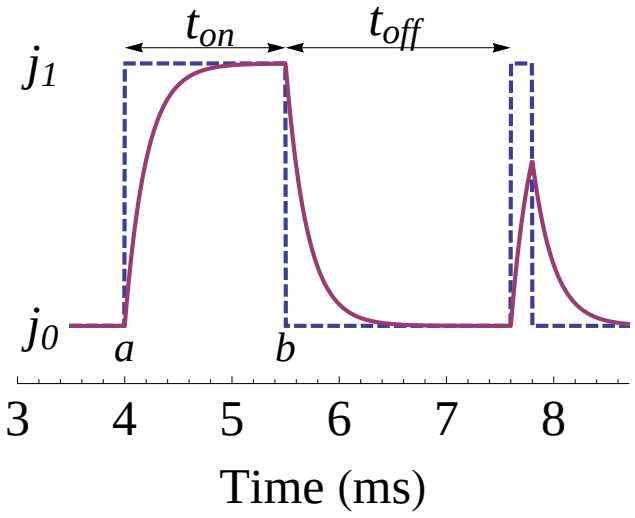

Figure 2.4: The simulated input step pulse signal (blue, dashed) is overlayed on the simulated output of our preamplifier, Eq. 2.29, (purple, solid). For this plot, $j_1 = 60$pA, $j_0 = 10$pA, and $\tau = 0.2$ms. The first pulse lasts $1.5\text{ms} = b - a$, while the second pulse lasts 0.2ms (equal to the time-constant of the preamplifier). Reprinted with permission from reference [30], Copyright 2014 American Chemical Society.

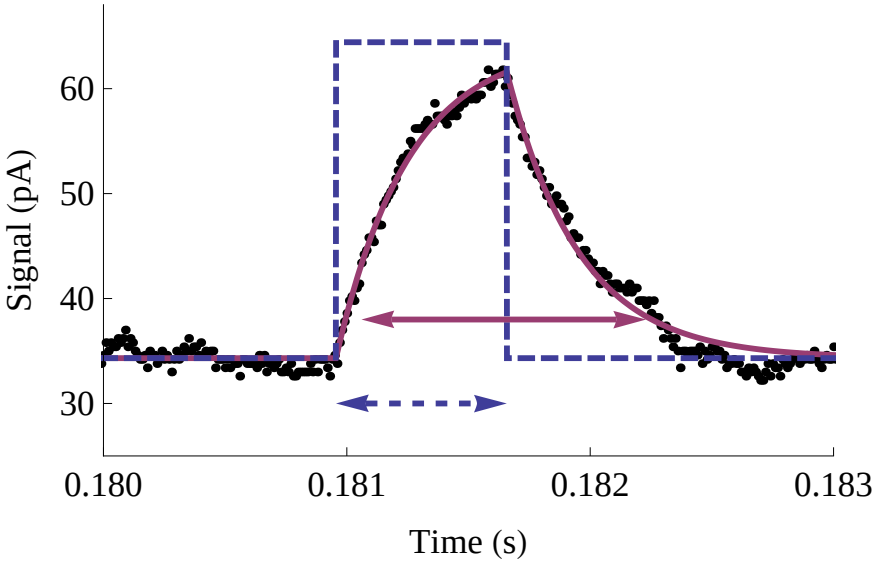

Figure 2.5: Equation 2.29 is used to create a fit (purple) of a single switching event (black) with fit parameters j_0, j_1, τ, a, and b. The value of j_1 from the fit is used to construct the step pulse (dashed blue). The arrows represent the residence time according to the discriminator level (purple arrow, at ∼40pA) verses its true magnitude (dashed blue arrow). The switching event comes from a high-resolution trace (10 μs steps) from a point on L1 at a sample bias of 2 V and a setpoint current of ∼35 pA. Reprinted with permission from reference [30], Copyright 2014 American Chemical Society.

exceed 100% whilst also becoming very dependent on the location of the discriminator level, as seen in Fig 2.5.

2.3 Implementation

2.3.1 On-Level Determination

Five peaks of varying heights were chosen from every trace on both up-switching lobes (L1 and L3). Each of these peaks were fit with Eq 2.29, producing 5 fit parameters: j_0, j_1, τ, a, and b. For each trace, the values of each parameter were compared across the 5 peak fits. Aside from a and b, which will vary from pulse to pulse, the parameters agreed very well with one another. Figure 2.6 shows the deviations seen in j_1. This reaffirms the fact that (1) the setpoint current, j_0, remained constant throughout the measurement and (2) that the system is governed by an instrumental rise-time, τ. More importantly, the fits demonstrate that up-switching is dichotomous with a singular "on" state level, j_1. Traces taken at low, preresonant biases further demonstrate dichotomous up-switching (Fig 2.7).

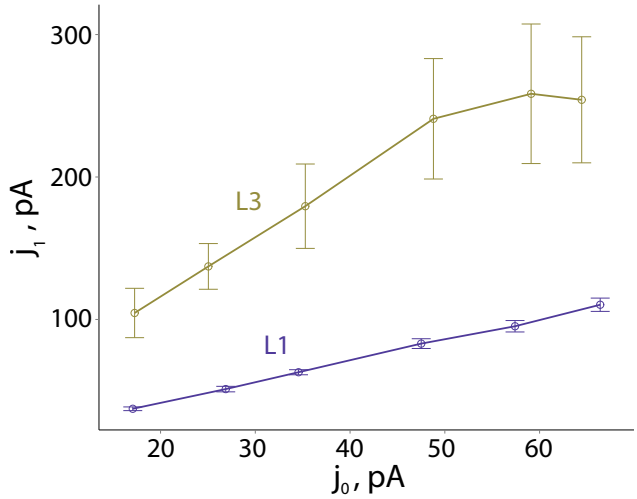

Figure 2.6: The correlations between corrected j_1 and j_0 for L1 and L3 for the high resolution traces are linear with a slope of 1.5±.02 and 3.4±.4, respectively. The error bars are the standard devations of j_1. Note the small deviations in L1's corrected j_1 distribution ($\sim$ 4%). The large deviations on L3 ($\sim$ 16%) are likely due the high j_1 tunneling current. The tip perturbs the molecule more at higher current levels. Reprinted with permission from reference [30], Copyright 2014 American Chemical Society.

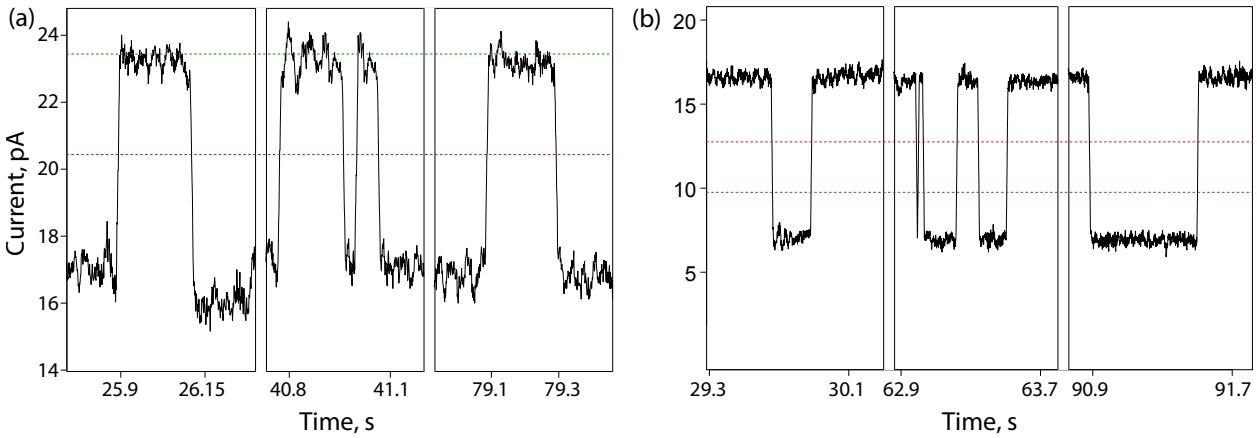

Figure 2.7: At lower biases, the on-time increases while the onrate decreases. (a) and (b) are typical low bias traces. Specifically, both are high-resolution traces taken at a sample bias of 1.7 V and a tunneling current of ∼17 pA. (a) Positioning the tip over L1 shows dichotomous up-switching while the same over L2 (b) shows dichotomous down-switching. A 100μs moving average was applied to both traces to better show this switching. The red and green dashed lines signify the "on" and "off" discriminator levels. Reprinted with permission from reference [30], Copyright 2014 American Chemical Society.

2.3.2 On-Time Correction

Due to noise within the trace, switches were counted through the use of two discriminator levels. For a switch to be counted, the signal must first pass the "on" discriminator and then fall pasted the "off" discriminator (See Fig. 2.7). The "on" discriminator level, $V_{a'}$, was placed at a level 4σ above the setpoint PHD. The "off" discriminator level, $V_{b'}$, was placed 3 pA below the "on" discriminator (towards the setpoint PHD). For these traces, 3 pA was chosen as it was larger than the typical current noise in the trace. Had only one discriminator been used, the noise in the trace would have resulted in false counts.

The method used to count the number of switches produced a list of times, a' and b', at which the trace passed above the "on" and then fell below the "off" discriminator, respectively. As shown earlier, the difference between these two values gives you t_{on} but with significant errors. However, like j_1, these residence times can be corrected using Eq (2.29).

Eq (2.29) is simplified slightly by looking only during the rise and fall of the peak.

$$V_0(t) = \begin{cases} (j_1 - j_0)(-e^{-\frac{t-a}{\tau}}) + j_0 & \text{if } a < t < b \\ (j_1 - j_0)(-e^{-\frac{t-a}{\tau}} + e^{-\frac{t-b}{\tau}}) + j_0 & \text{if } t > b \end{cases} \tag{2.30}$$

Then, assuming values for j_0, j_1, and τ (taken from the average of the five fits of various peaks), one can plug $t{=}a'$ and $V_0(t){=}V_{a'}$ into (2.30a) and solve for a. Using this solution, b is determined by plugging in $t{=}b'$ and $V_0(t){=}V_{b'}$ into (2.30b). The corrected residence times are more accurate than just using the discriminator method. However, there is some uncertainty in the corrected residence time due to uncertainties in j_0, j_1, and τ.

The analysis and demonstration of this single-electron switch represents a step toward controlling the fundamental units of a molecule. Given the quantum nature of this device, techniques like spin-polarized STM could allow for the controlled manipulation of a unit of quantum information.

Chapter 3

System Improvements

The following sections describe the various ways experiments and the equipment used in these experiments have been developed and improved. Improvements are continuously being made and further progress is expected over the course of my graduate career.

3.1 Parabolic Mirror Alignment

The homebuilt UHV cryogenic STM used for the various experiments is unique due to its inclusion of a piezo-controlled parabolic mirror. This mirror encircles the tip-sample junction and is used for the focusing and/or collection of light. The focus of this parabolic

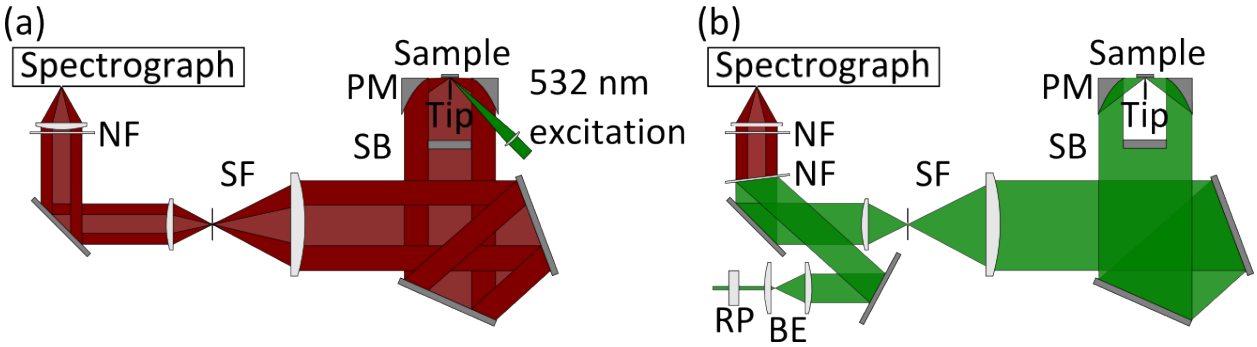

Figure 3.1: Excitation geometries with the excitation laser shown in green and the Raman signal in red. (a) Excitation at 45°. (b) Excitation via the Parabolic Mirror. NF = 532 nm notch filter, SF = spatial filter with 100 μm pinhole, SB = scanner base, PM = parabolic mirror, RP = radial polarizer, BE = beam expander.

mirror is positioned exactly at the junction of the STM, where the metallic tip meets the conductive sample, allowing light scattered from this region to be collected, collimated, and directed out of the main vacuum chamber. This scheme benefits from a relatively high collection efficiency, when compared to a standard 1" lens, and diffraction-limited, chromatic aberration-free focusing of light. This makes a parabolic mirror ideal for the focusing and collection of ultrafast laser pulses which undergo dispersion when passing through refractive optics. However, correctly aligning the parabolic mirror onto the STM tip apex is a complex process. To better understand the excitation and collection geometry, the optical setup (Fig. 3.1) was simulated using Zemax OpticStudio^{TM} 14.2.

3.1.1 Ray Tracing Simulation

The model of the collection line (Figures 3.2 and 3.3) contains the essential elements of the experimental detection line. Light, represented by blue ray lines, is emitted or is scattered from a sphere or spherical cone. Using the non-sequential ray tracing, rays either reflect off of the ⌀1.384" parabolic mirror or are absorbed by the three-legged base of the scanner. The rays reflected off of the parabolic mirror are sent past the base of the scanner. The shadow cast by the base of the scanner produces the three-lobed image seen in Figures 3.4 and 3.5. After the scanner base, the rays travel ∼1.8 m before entering a spatial filter (SF) consisting of a ⌀2" achromatic doublet lens (f = 75 mm, Thorlabs AC508-075-A), a 100 μm pinhole, and a ⌀1" achromatic double lens (f = 30 mm, Thorlabs AC254-030-A), giving a total magnification power of 0.4. The ⌀0.55" image travels ∼ 0.27 m before being focused onto a detector with a ⌀1" achromatic doublet lens (f = 100 mm, Thorlabs AC254-100-A). The models of the parabolic mirror and the scanner base were created in Autodesk®Inventor®and imported into Zemax. The lenses were taken from ThorLabs' Zemax library.

	Object Type	Comment	Ref Object	Inside Of	X Position	Y Position	Z Position	Tilt About X	Tilt About Y	Tilt About Z	Material
1	Source Ray	5.08 is the focus	0	0	0.000	0.000	60.000	0.000	0.000	0.000	-
2	Cone		0	0	0.000	0.000	0.000	0.000	0.000	0.000	
3	Cylinder Volume	SAMPLE	0	0	0.000	0.000	-1.000E-003	0.000	0.000	0.000	
4	CAD Part: Autodesk Inventor®	ParabolicMirror2_mm.ipt	0	0	0.000	0.000	-5.080	270.000	-30.000	0.000	
5	CAD Part: Autodesk Inventor®	scanner_base_mm.ipt	0	0	0.000	0.000	40.000	270.000	0.000	0.000	
6	Detector Rectangle	after base	0	0	0.000	0.000	65.000	0.000	0.000	0.000	
7	Detector Rectangle	before spatial filter	0	0	0.000	0.000	1780.000	0.000	0.000	0.000	
8	Standard Lens	surfaces 2-3	0	0	0.000	0.000	1800.000	0.000	0.000	0.000	E-BAF11
9	Standard Lens	surfaces 3-4	8	0	0.000	0.000	20.000	0.000	0.000	0.000	N-SF11
10	Cylinder Pipe	pinhole, at 64mm	9	0	0.000	0.000	64.000 V	0.000	0.000	0.000	
11	Standard Lens	surfaces 5-6	9	0	0.000	0.000	99.500	180.000	0.000	0.000	N-BAF10
12	Standard Lens	surfaces 6-7	11	0	0.000	0.000	12.000	0.000	0.000	0.000	N-SF6HT
13	Standard Lens	surfaces 8-9	8	0	0.000	0.000	370.000	0.000	0.000	0.000	N-BK7
14	Standard Lens	surfaces 9-10	13	0	0.000	0.000	4.000	0.000	0.000	0.000	SF5
15	Detector Rectangle	after spatial filer	10	0	0.000	0.000	40.000	0.000	0.000	0.000	
16	Detector Rectangle	before final lens	14	0	0.000	0.000	-10.000	0.000	0.000	0.000	
17	Detector Rectangle	ccd	14	0	0.000	0.000	100.000	0.000	0.000	0.000	

Figure 3.2: The component editor in Zemax OpticStudio 14.2 for the parabolic detection line.

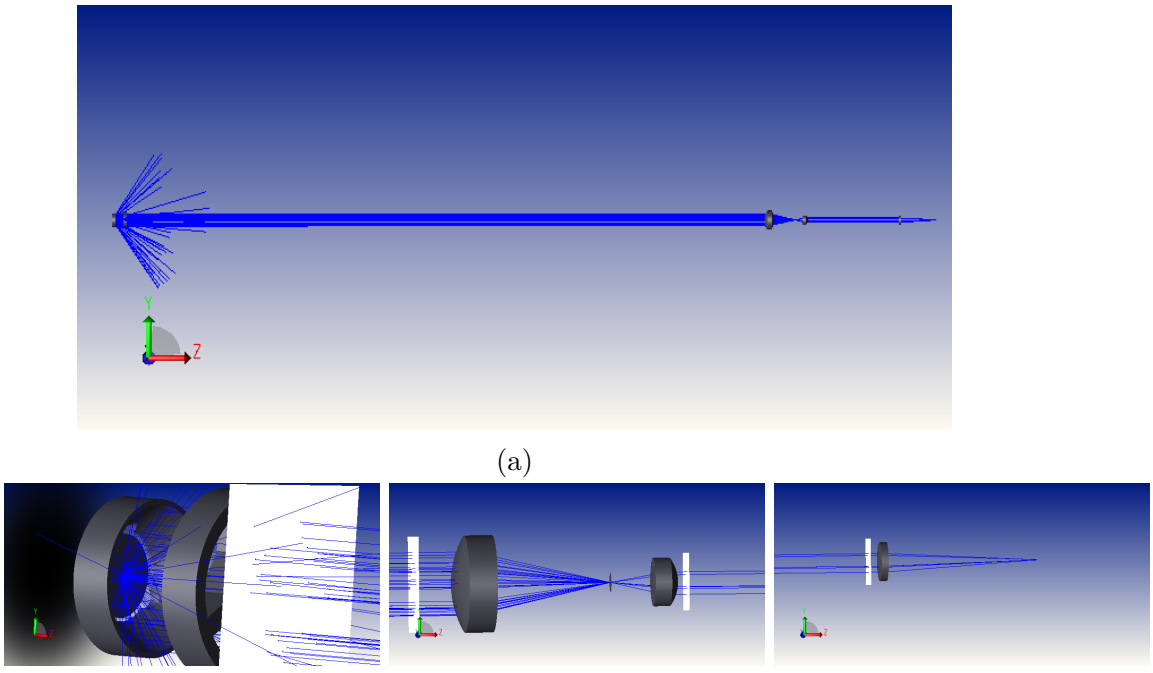

(a)

(b) (c) (d)

Figure 3.3: Model of parabolic detection line. (a) View of the full model. (b) Scanner body, angle view. Point or volume ellipse source is placed at the focus of the parabolic mirror. (c) Spatial Filter and pinhole. (d) Final focusing lens. The white squares are detectors and blue lines represent calculated rays.

3.1.2 Impact of the source

Spherical Source

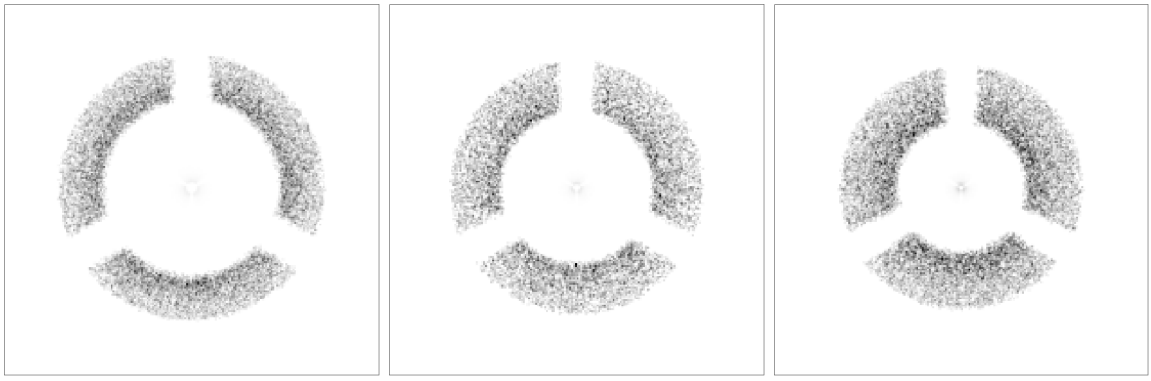

(a) 10μm High (b) at focus (c) 10μm Low

Figure 3.4: The position of a spherical source (radius = 5 μm) on the detected image 1.78 m away. Moving the source higher brings the source closer to the sample. Moving the source lower brings the source down the shaft of the tip.

The size and shape of the image provides information about where the scattering source is with respect to the focus of the parabolic mirror. For instance, when the scattering source is positioned above (below) the focus of the parabolic mirror, the scattered image diverges (converges) (See Fig. 3.4). The collapsing of the image suggests scattering from the tip shaft while the expanding of the image suggests scattering from the sample. In reality, we often can see mixing of these images, suggesting that both the tip shaft and sample are participating in the scattering.

As the radius (r) of the spherical source is increased (see Fig 3.5), the lobes in the image grow and become blurry while the cutoff between lobes become more radial. This change in the angle of the edge of lobes is also seen in Fig 3.4c.

Parabolic Excitation Geometry

Focusing onto the junction with the parabolic mirror rather than with a 1" lens at 45° normal to the sample surface allows excitation with a much shallower incidence angles (4 to 30°). Analysis of this geometry revealed that the resulting image now included both scattering

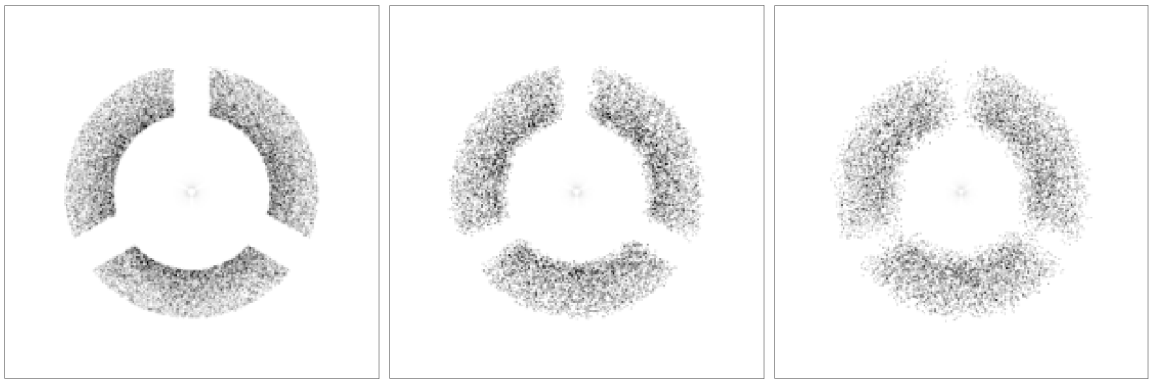

(a) r = 1 μm (b) r = 10 μm (c) r = 20 μm

Figure 3.5: The detected image 1.78 m away with various source sizes at the focus.

from the tip (modeled by a sphere) and reflections from the sample. The scattering from the tip gives the well-understood 3-lobed image (Fig. 3.4) while reflection from the sample gives a 6-lobed image. The 6 lobes result from the beam passing by the base of the scanner twice, casting two shadows (Fig 3.6). This 6-lobed image is readily observed in the experiment both before and after the spatial filter. However, after the signal passes through the notch filter, only the scattered 3-lobed image remains. This suggests that the sample itself produces no Raman shifted photons and that the observed broad Raman background is from the tip, as initially thought.

This alignment is very sensitive to errors in the beam propagation angle. If the excitation beam angle is too large, resulting from either poor collimation or alignment errors, the beam will not hit the tip apex. Instead, it will only reflect off of the sample, producing only the 6-lobed image.

3.1.3 Parabolic Alignment Tool

Aligning the parabolic mirror to the tip apex is critical for optimizing the collection of SM-TERS photons. However, the alignment process can at times be difficult and confusing. The parabolic alignment tool (Fig 3.7) was created in Wolfram Mathematica®10.2 to help guide us in positioning the parabolic mirror. It simulates the electro-luminescence (EL)

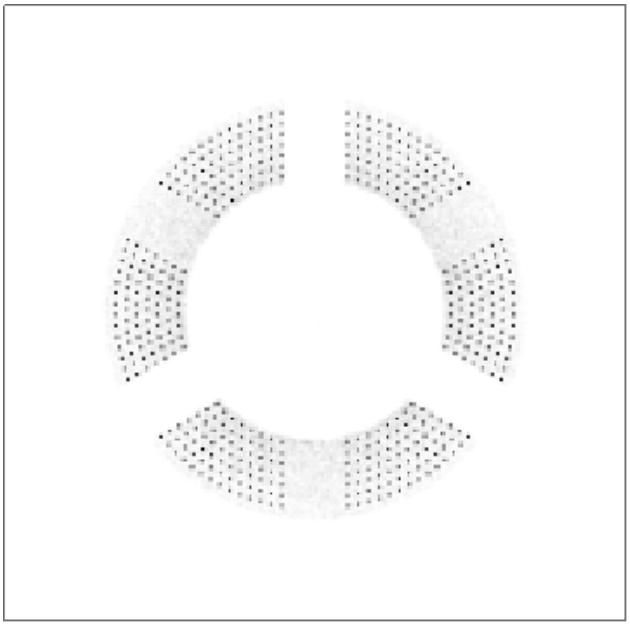

Figure 3.6: Detected image before the spatial filter using parabolic excitation. The 6-lobe structure, consisting of highly ordered rays, is from reflections off of the sample. The diffuse 3-lobe background is from lambertian scattering off of the sphere, r = 1 μm.

image on the ccd plane. The tool includes 3 axis controls, allowing the user to simulate how the EL image will change when the mirror is translated in any given direction. When a mirror position is requested, the tool imports a previously save PNG image displaying a density plot of the simulated CCD image. These simulations, in turn, were produced using a slight variation of the previously described Zemax OpticStudio^{TM} 14.2 model of the parabolic mirror detection line. Since the spatial filter is not used during parabolic mirror alignment, the spatial filter is omitted from the ray-tracing simulation.

3.2 Load-Lock System

Given the importance of the STM tip in TERS experiments and the uncertainty in how the tip geometry contributes to the TERS signal, it is critical to be able to continually test new tip geometries as our understanding of the TERS process improves. Furthermore, the properties of the molecule itself, such as its Raman scattering cross-section, dipole alignment, and coupling to the surface, are critical to obtaining spatially resolved TERS. The original design

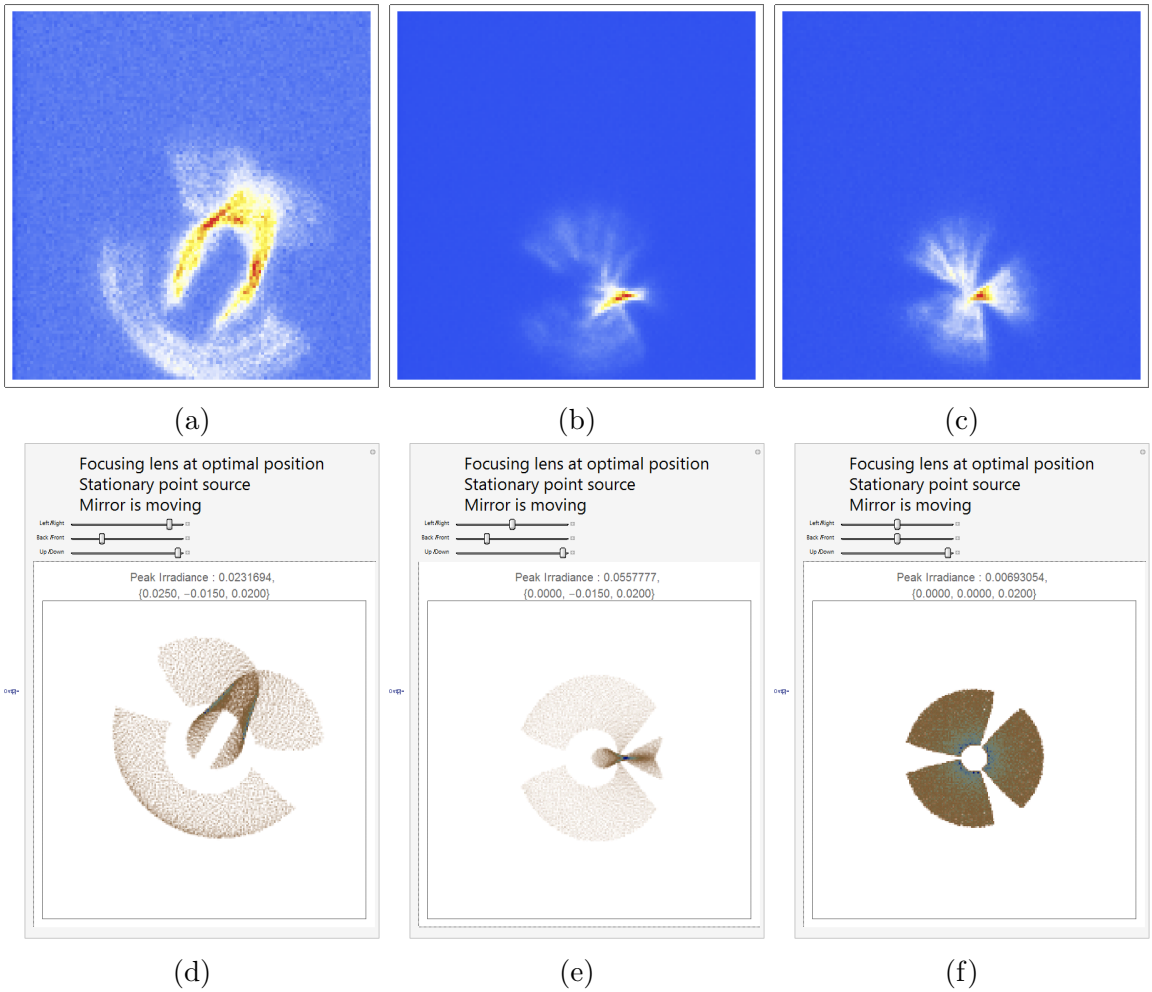

Figure 3.7: Parabolic Alignment Tool aids in positioning the parabolic mirror. The experimentally observed images, (a)-(c), are recreated using the 3-axis control of the tool, (d)-(f).

of the home-built cryogenic UHV-STM allowed for the storage of 7 samples, 40 STM tips, and 2 molecular dosers. However, adding new tips to the chamber or a new molecule to the doser originally required bringing the chamber from 5×10^{-11} torr to atmosphere, resulting in long instrument down-times as well as unwanted stress to the chamber itself, especially to its various delicate filaments. In an effort to improve the flexibility and capabilities of our STM, a load-lock system has been added that enables the changing of tips, samples, and molecules with relative ease and minimal impact to the chamber.

In the original design, unused tips and samples were stored on a rotating carousel affixed to the inside face of a 6" CF flange via a mounting rod and screws. The new load-lock

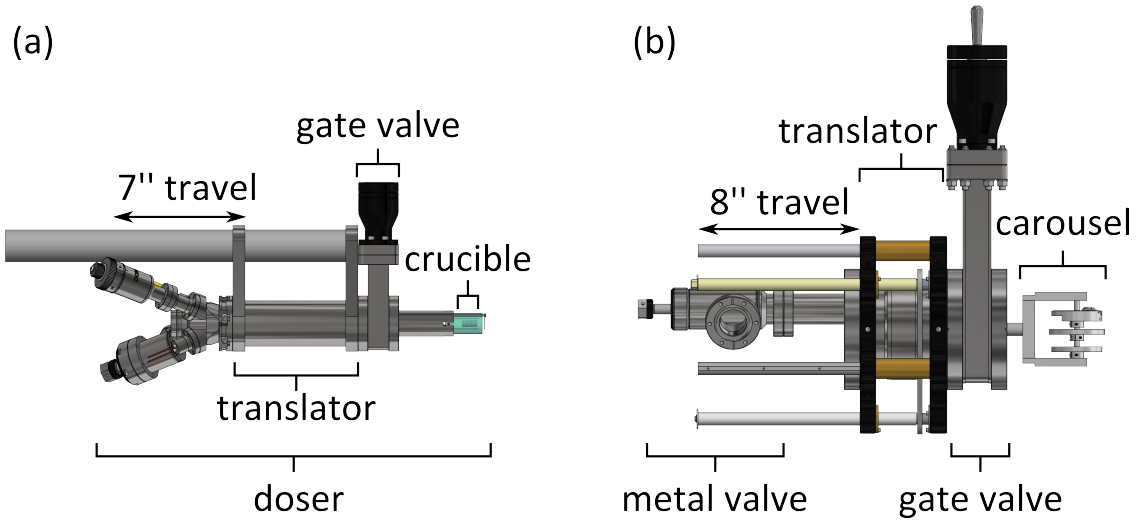

Figure 3.8: Schematic of the tip/sample and doser loadlocks. (a) The molecular doser is placed on 2.75" manual single-axis translator with 7" of travel, attached to the chamber via a 2.75" gate valve. (b) A 6" gate valve and a 6" bellows-sealed linear translator with 8" of travel is placed between the chamber and the carousel's base flange. The rod connecting the carousel to the base flange is lengthened to compensate for the additional width of the compressed translator and gate valve.

worked off of this design by inserting a 6" gate valve and a 6" bellows-sealed linear translator (McAllistor BLT63) between the main chamber and the original 6" CF flange. The original flange is modified with a protruding 2.75" CF flange, allowing for the attachment of a 2.75" All-Metal angle valve and the mounting rod is lengthened to compensate for the additional length of the gate valve and compressed translator. To exchange samples and tips, the load-lock translator is fully extended to retract the carousel from the main chamber. The gate valve is then closed to isolate the carousel from the main chamber, allowing this isolated section to be brought up to ambient pressure by leaking dry nitrogen gas through the All-Metal angle valve. The carousel flange, with the stocked carousel, can then be removed from the chamber and its sample/tip supply restocked. The carousel flange can then be reattached and pumped out by the external pumping system (explained later). The pumping, baking, and degassing of the load-lock and external pumping system required to reach 9×10^{-10} torr takes approximately 5 days. Once the pressure reaches the desired level, the load-lock gate valve can be opened, followed quickly by the closing of the load-lock All-Metal angle valve.

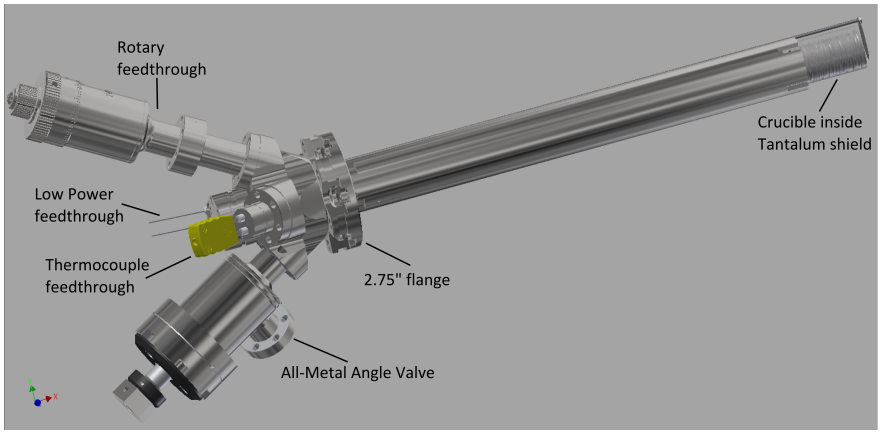

Figure 3.9: Schematic of the molecular doser. The doser length (12.5") had to be increased because the of the length of the fully compressed translator (6.18").

The base pressure of the main chamber does rise to $\sim 1 \times 10^{-10}$ but can be lowered over time with the help of the main chamber's titanium sublimation pump (TSP) and ion pump.

To enable the quick exchange of molecules that can be dosed or evaporated onto our sample, a retractable and removable molecular doser (evaporator) is required. Due to the length of the fully compressed linear translator and gate valve, the doser originally would no longer extend fully into the main chamber. Although there exist commercially available retractable dosers (Kentax TCE-BS), all of its heating crucibles were slightly displaced from the flange's central axis. Due to the small opening in the scanner's shield for the passing of the molecular beam, an on-axis evaporator is required. Furthermore, a homebuilt doser would allow us to completely control its design and maintenance.

The design of the homebuilt doser was kept simple. A rotary feedthrough (for shutter control), a low-power feedthrough (for supplying the heating current), a k-type thermocouple feedthrough, a blank mini-flange, and an All-Metal Angle Valve were installed onto a 2.75" Flange Multiplexer (Kimball Physics MCF275-FlgMplxr-Cr1A5). Tungsten wire ($\varnothing$0.02") is wrapped along the threads of an alumina crucible, which was previously cut and threaded with the help of members of the Wilson Ho Lab at UC Irvine following established procedures[37]. The wrapped crucible is suspended via the tungsten wire between two 2" long 0-80 tantalum threaded rods, which, in turn, were connected to alumina-insulated copper

wires that lead to the low-power feedthrough. When current (< 4 Amps) is applied to this continuous connection, the tungsten wire heats the alumina crucible holding the ∼50 mg of the molecule to be dosed. The tantalum/alumina assembly is supported by a small aluminum base, which, in turn, is supported by two 14" long 6-32 thread stainless steel rods that are screwed into an adapter plate on the bottom blank mini-flange. The crucible and its immediate support structure is enclosed within a custom built cylindrical tantalum shield (OD = 0.5") with a small 0.25" molecular beam exit hole. The rotary feedthrough rotates a long 2-56 threaded rod attached to a tantalum shutter. The k-type thermocouple is placed in contact with a small recess on the bottom of the crucible. The internal body of the doser in enclosed within a stainless steel tube (OD = 0.625", ID = 0.505") to ensure the body's straightness. Exchanging the molecular doser is accomplished using the same protocol as the sample/tip exchange by using its own smaller gate valve and All-Metal valve.

3.2.1 Pumping Station

An external pumping system capable of attaining UHV is needed in order to use the load-lock. As discussed above, this pumping system must be able to reach at least 9×10^{-10} torr and must be portable. To reach this pressure, the station (Fig. 3.10) is equipped with a scroll backing pump, a turbomolecular pump, a ion pump, and a titanium sublimation pump (TSP). To ensure the system is portable, the whole system is supported by an aluminum t-slotted frame terminated by a set of casters. Any remaining controllers are held in a separate 19" portable rack.

The chamber is brought to UHV using standard vacuum techniques. To prepare the system for pumping, the main gate valve is closed. The scroll pump then pumps out the section containing the turbo pump to < 50 mTorr. The turbo pump can then be safely started in preparation for opening the gate valve. However, before the gate valve can be opened, the chamber is first pumped down to 5 mTorr with a liquid nitrogen sorption pump through the chamber's All-Metal valve. Once 5 mTorr is reached, the All-Metal valve is closed and the

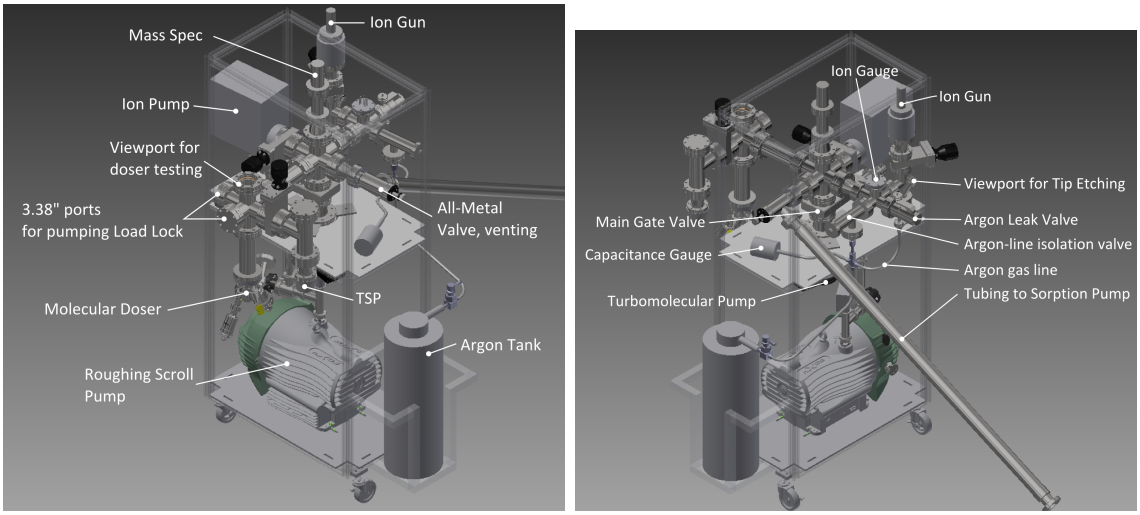

(a) Left Side (b) Right Side

Figure 3.10: The multipurpose Pumping Station is used for the testing of molecular dosing conditions or for pumping out the main chamber's load lock (a) as well as for the field-directed ion sharpening of metallic tips (b). The important components for these tasks are labeled.

main gate valve is quickly opened. The chamber pressure will soon drop to below 10^{-5} Torr, allowing for the use of the ion gauge. To reach 9×10^{-10} Torr, the chamber is wrapped with a combination of flexible silicone rubber heat tapes (BriskHeat BS0) affixed with heat-resistant tape and heat sheets (McMaster-Carr), all of which is covered with aluminum foil.

Tip Preparation

The exact morphology of the TERS tip that can produce sub-nanometer spatial resolution[25] is still not well understood. However, it is generally considered that a silver or gold tip with an apex radius of curvature < 20 nm is required due to the plasmonic properties of silver and gold and the field enhancement provided by the sharp apex.[38] Since the measured signals are often very small, it is desirable to reduce the background signal as much as possible. Raman and photoluminescence from metal junctions or metal nanoparticles may contribute a SERS signals at positions remote from the tip apex itself, potentially overwhelming signals from the target molecule via TERS.[39] This sometimes unwanted metal signal can likely be reduced by limiting the number of scattering sites and "hot spots" in the focal volume of

the laser. In an attempt to produce both sharp (< 10 nm) and smooth tips, we investigated field-directed sputter sharpening (FDSS) of Ag and Au tips.

Traditionally, silver, gold, and tungsten STM tips are produced through electro-chemical etching. To simplify and standardize the manufacture of Ag and W tips, our lab uses a two-stage semi-automatic electro-chemical etching procedure.[40] This technique can produce relatively smooth and sharp Ag and W tips, with a radius of curvature < 100 nm. Nevertheless, the tip surface is often rough and the apex radius of curvature is usually larger than 20 nm, a deviation from the ideal TERS tip.

There are numerous other techniques for producing sharp STM tips. Schumucher et.al.[41] introduced and demonstrated the power of FDSS on platinum-iridium, tungsten, and hafnium diboride tips, achieving nanometer and sub-nanometer radii of curvature. In FDSS, a positively-biased (100 - 500 V) electrochemically-etched tip is sputtered with 500 - 2000 eV Ar^+ ions. The ions are fired along the long axis of the tip, leading to a shallow angle of incidence. The bias applied to the tip creates an enhanced electrostatic potential at the tip apex. This potential gradient works to deflect incident Ar^+ ions from the apex, preferentially sputtering the surface below the apex (Fig. 3.11f).

Aside from applying this technique to new materials (e.g. Ag and Au), studies were done to enable batch fabrication of tips. Initially, multiple tips, arranged in a ring < 10 mm apart with a single tip in the center, were simultaneously sputtered via FDSS using the ion gun pictured in Figure 3.10. These initial tests showed very limited sharpening of Ag tips. Tips positioned in the center were found to be only ones that saw any substantial improvements. Finite-element simulations revealed that the required potential gradient is drastically reduced once multiple tips were held in the biased tip holder. This reduced gradient is unable to deflect incident ions to the degree necessary for sharpening and smoothing (Fig. 3.11(a-c)). However, when grounding plates are included between adjacent tips, the required potential gradient is recovered, deflecting incident ions (Fig. 3.11(d-f)). A grounding plate and tip holder were designed and built to allow for FDSS of 7 tips simultaneously.

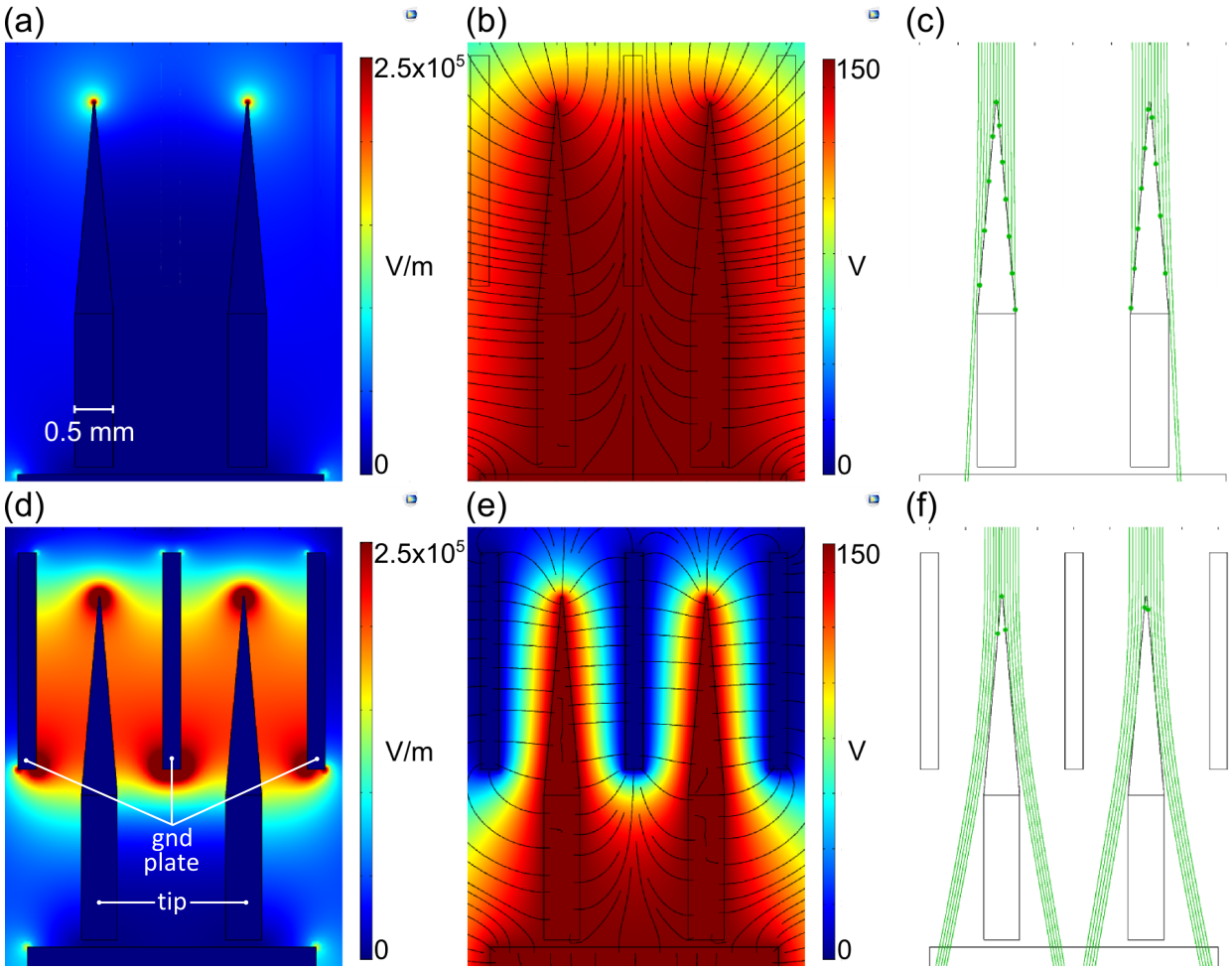

Figure 3.11: Argon ion particle trajectory simulation for batch FDSS of STM tips. Without grounding plates, the electric field (a) is asymmetric about the tip and the electric potential (b, colors) is fairly constant between adjacent tips. Electric field lines are shown to again show asymmetric field. The associated ion trajectories show very weak FDSS (c). The addition of grounding plates enhances the electric field at the apex (d) and restores the electric potential gradient between tips, yeilding good FDSS (f). Tip/Bottom plate bias = 150 V, Ion beam energy = 2000 eV, cone half angle = 5°, tip radius of curviture = 50 nm.

Bibliography

[1] Song, Z.; Zhou, H. *Energy & Environmental Science* **2013**, *6*, 2280.

[2] Shirakawa, H.; Louis, E. J.; MacDiarmid, A. G.; Chiang, C. K.; Heeger, A. J. *Journal of the Chemical Society, Chemical Communications* **1977**, 578.

[3] Bachtold, A.; Hadley, P.; Nakanishi, T.; Dekker, C. *Science* **2001**, *294*, 1317–20.

[4] Frank, S. *Science* **1998**, *280*, 1744–1746.

[5] Kwiat, M.; Cohen, S.; Pevzner, A.; Patolsky, F. *Nano Today* **2013**, *8*, 677–694.

[6] Hermosa, C.; Vicente Álvarez, J.; Azani, M.-R.; Gómez-García, C. J.; Fritz, M.; Soler, J. M.; Gómez-Herrero, J.; Gómez-Navarro, C.; Zamora, F. *Nature Communications* **2013**, *4*, 1709.

[7] Aviram, A.; Ratner, M. A. *Chemical Physics Letters* **1974**, *29*, 277.

[8] Martel, R.; Schmidt, T.; Shea, H. R.; Hertel, T.; Avouris, P. *Applied Physics Letters* **1998**, *73*, 2447.

[9] Aviram, A.; Joachim, C.; Pomerantz, M. *Chemical Physics Letters* **1988**, *146*, 490–495.

[10] Donhauser, Z. J.; Mantooth, B. a.; Kelly, K. F.; Bumm, L. a.; Monnell, J. D.; Stapleton, J. J.; Price Jr, D. W.; Rawlett, a. M.; Allara, D. L.; Tour, J. M.; Weiss, P. S. *Science* **2001**, *292*, 2303–7.

[11] Moresco, F.; Meyer, G.; Rieder, K.-H.; Tang, H.; Gourdon, A.; Joachim, C. *Physical Review Letters* **2001**, *86*, 672–675.

[12] Huang, T.; Zhao, J.; Feng, M.; Popov, A. a.; Yang, S.; Dunsch, L.; Petek, H. *Nano Letters* **2011**, *11*, 5327–32.

[13] Schirm, C.; Matt, M.; Pauly, F.; Cuevas, J. C.; Nielaba, P.; Scheer, E. *Nature Nanotechnology* **2013**, *8*, 645–8.

[14] Kumagai, T.; Hanke, F.; Gawinkowski, S.; Sharp, J.; Kotsis, K.; Waluk, J.; Persson, M.; Grill, L. *Nature Chemistry* **2013**, *6*, 41–46.

[15] Pop, E. *Nano Research* **2010**, *3*, 147–169.

[16] Shank, C. V. *Applied Physics Letters* **1974**, *24*, 373.

[17] Zewail, A. H. *The Journal of Physical Chemistry A* **2000**, *104*, 5660–5694.

[18] Petek, H. *ACS Nano* **2014**, *8*, 5–13.

[19] Wu, S. W.; Ogawa, N.; Ho, W. *Science* **2006**, *312*, 1362–5.

[20] Berndt, R.; Gaisch, R.; Schneider, W.; Gimzewski, J.; Reihl, B.; Schlittler, R.; Tschudy, M. *Physical Review Letters* **1995**, *74*, 102–105.

[21] Neacsu, C.; Dreyer, J.; Behr, N.; Raschke, M. *Physical Review B* **2006**, *73*, 193406.

[22] Sonntag, M. D.; Klingsporn, J. M.; Zrimsek, A. B.; Sharma, B.; Ruvuna, L. K.; Van Duyne, R. P. *Chemical Society Reviews* **2014**, *43*, 1230–47.

[23] Sonntag, M. D.; Klingsporn, J. M.; Garibay, L. K.; Roberts, J. M.; Dieringer, J. a.; Seideman, T.; Scheidt, K. a.; Jensen, L.; Schatz, G. C.; Van Duyne, R. P. *The Journal of Physical Chemistry C* **2012**, *116*, 478–483.

[24] Steidtner, J.; Pettinger, B. *Physical Review Letters* **2008**, *100*, 236101.

[25] Zhang, R.; Zhang, Y.; Dong, Z. C.; Jiang, S.; Zhang, C.; Chen, L. G.; Zhang, L.; Liao, Y.; Aizpurua, J.; Luo, Y.; Yang, J. L.; Hou, J. G. *Nature* **2013**, *498*, 82–86.

[26] Lee, J.; Perdue, S. M.; Rodriguez Perez, A.; Apkarian, V. A. *ACS Nano* **2014**, *8*, 54–63.

[27] Love, J. C.; Estroff, L. A.; Kriebel, J. K.; Nuzzo, R. G.; Whitesides, G. M. *Chemical Reviews* **2005**, *105*, 1103–69.

[28] Sasaki, S. S.; Zhang, Y.-n.; Dey, S.; Tallarida, N.; El-Khoury, P. Z.; Apkarian, V. A.; Wu, R. *The Journal of Physical Chemistry C* **2014**, *118*, 29287–29293.

[29] Blum, A. S.; Kushmerick, J. G.; Long, D. P.; Patterson, C. H.; Yang, J. C.; Henderson, J. C.; Yao, Y.; Tour, J. M.; Shashidhar, R.; Ratna, B. R. *Nature Materials* **2005**, *4*, 167–172.

[30] Lee, J.; Tallarida, N.; Rios, L.; Perdue, S. M.; Apkarian, V. A. *ACS Nano* **2014**, *8*, 6382–6389.

[31] Gardiner, C. *Handbook of Stochastic Methods for Physics, Chemistry and the Natural Sciences*; Springer: Berlin, 1997.

[32] Lee, J.; Perdue, S. M.; Perez, A. R.; El-Khoury, P. Z.; Honkala, K.; Apkarian, V. a. *The Journal of Physical Chemistry. A* **2013**, *117*, 11655–64.

[33] Chen, F.; Hihath, J.; Huang, Z.; Li, X.; Tao, N. *Annual Review of Physical Chemistry* **2007**, *58*, 535–564.

[34] Gouterman, M. *The Journal of Chemical Physics* **1972**, *56*, 4073.

[35] McConnell, H. M. *The Journal of Chemical Physics* **1961**, *34*, 13.

[36] Penfold, T.; Worth, G. *Chemical Physics* **2010**, *375*, 58–66.

[37] Brown, K. A.; Ho, W. *Review of Scientific Instruments* **1995**, *66*, 5371.

[38] Huang, T. X.; Huang, S. C.; Li, M. H.; Zeng, Z. C.; Wang, X.; Ren, B. *Analytical and Bioanalytical Chemistry* **2015**, 8177–8195.

[39] Tallarida, N.; Rios, L.; Apkarian, V. a.; Lee, J. *Nano Letters* **2015**, *15*, 6386–6394.

[40] Sasaki, S. S.; Perdue, S. M.; Perez, A. R.; Tallarida, N.; Majors, J. H.; Apkarian, V. A.; Lee, J. *Review of Scientific Instruments* **2013**, *84*, 096109.

[41] Schmucker, S.; Kumar, N.; Abelson, J.; Daly, S.; Girolami, G.; Bischof, M.; Jaeger, D.; Reidy, R.; Gorman, B.; Alexander, J.; Ballard, J.; Randall, J.; Lyding, J. *Nature Communications* **2012**, *3*, 935.